

Surface Trap for Ytterbium Ions

by

Jonathan A. Campbell

B.S., Arabic & German (1996)

United States Military Academy

Submitted to the Department of Physics in Partial Fulfillment
of the Requirements for the Degree of Master of Science

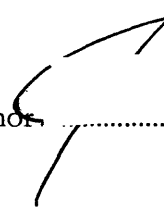
at the

Massachusetts Institute of Technology

June 2006

© 2006 Massachusetts Institute of Technology
All rights reserved

Signature of Author.....



Department of Physics
May 12, 2006

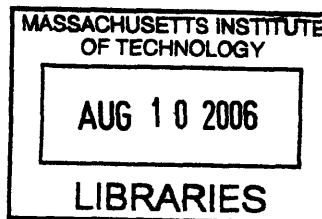
Certified by.....

Vladan Vuletić
Lester Wolfe Associate Professor of Physics
Thesis Supervisor

Accepted by.....

Thomas J. Greytak
Professor of Physics
Associate Department Head for Education

ARCHIVES



Surface Trap for Ytterbium Ions

by

Jonathan A. Campbell

Submitted to the Department of Physics
May 12, 2006 in Partial Fulfillment of the
Requirements for the Degree of Master of Science in
Physics

ABSTRACT

We conducted an experiment to load a shallow planar ion trap from a cold atom source of Ytterbium using photoionization. The surface trap consisted of a three-rod radio frequency Paul trap fabricated using standard printed circuit board techniques. The cold atom source was an isotope-selective magneto-optical trap of naturally-occurring Yb isotopes. The confining beams were provided by commercially-available ultra-violet diode lasers locked to an atomic reference using the Dichroic Atomic Vapor Laser Lock technique. We used photoionization from the Yb magneto-optical trap located within the region of the ion trapping potential.

Thesis Supervisor: Vladan Vuletić

Title: Lester Wolfe Associate Professor of Physics

Acknowledgements

MIT has been a humbling experience for me. Though I discovered physics isn't nearly as fun on the "left-hand" side of a bell curve, it will make me a much better physics instructor. I am in debt to Professor Vladan Vuletic for his willingness to take on board someone who was forever playing catch-up. We all benefit constantly from his experimental clarity and his willingness to allow us to "discovery learn." I have been helped by too many people on too many occasions to list them all, but my fellow graduate students, Marko Cetina and Andrew Grier are at the top of the list. Mine has been a decidedly junior role to these two brilliant physicists, and Marko's doggedness and Andrew's common sense have been responsible for every step forward this experiment has taken. Whenever I had a question (and there were many), I could count on Marko or Jon Simon for a ready explanation, and luckily for me, I could count on Andrew to explain their explanation to me. The entire Vuletic Group has a unique atmosphere—everyone shows a constant willingness to stop what they're doing to help someone fix or design or find or troubleshoot whatever they need. Our undergraduates, Brendan Shields, Thaned Pruttivarasin, and David Brown, have nobly accomplished key parts of this experiment while juggling a lot of other commitments. I am incredibly grateful to my wife, Victoria, as we struggled to mesh my schedule where the real work is done in the lab on campus with hers where the campus is a distraction and the real work must be done elsewhere. Sometimes it felt like we were on different planets. Luckily, though they came close a couple of times, the planets never collided, probably because we had first Jo Hulse and then Przemek Mieszkowicz to watch over our precious little girl, Anna, who is a constant source of smiles! Finally, I am grateful to the United States Army and the United States Military Academy Department of Physics for the wonderful opportunity to study here in the first place.

Table of Contents

ABSTRACT	2
ACKNOWLEDGEMENTS	3
TABLE OF CONTENTS	4
LIST OF FIGURES	5
LIST OF TABLES	6
ABBREVIATIONS	7
CHAPTER 1: INTRODUCTION	8
Surface Ion Traps	8
Why Ytterbium?	9
CHAPTER 2: EXPERIMENTAL SET-UP	12
Laser System	12
Laser Lock	14
Isotope Selectivity	16
Trapping Chamber	17
Magneto-Optical Trapping	18
Ionization	20
Ion Trapping	21
CHAPTER 3: RESULTS	28
Ion Detection	28
DC Offset	28
Trapping Ions	29
CHAPTER 4: DISCUSSION	33
APPENDIX A: MAGNETIC COILS	35
Gradient Coils	35
Bias Coils	36
APPENDIX B: RESPONSE TIMES	39
Ion Detector / High Voltage	39
UV LED	39
RF Voltage	39
Mechanical Shutter	40
SELECTED BIBLIOGRAPHY	41

List of Figures

Relevant energy level diagram of Ytterbium.....	9
Experiment's Optical Set-Up	12
Dichroic Atomic Vapor Laser Lock.....	15
Absorption Spectra experienced in Yb HCL.....	16
Trapping chamber.....	17
Magneto-Optical Trap.....	19
Emission Spectra of Ionizing LED.....	20
Radio Frequency Paul Trap	23
Planar Trap Design	26
Trap center height calculated as a function of ground-rf electrode ratio	27
Trapping Ions	29
Dependence of trap on increasing "dump time"	30
Dependence of Trap on Loading Time.....	31
Dependence of trap on Ion Storage Time	32
Magnetic Coils	35

List of Tables

Relative Abundance of Ytterbium Isotopes.....	10
Photoionization Levels	21

Abbreviations

BEM	Boundary Element Method
ECDL	External Cavity Diode Laser
DAVLL	Dichroic Atomic Vapor Laser Lock
DC	Direct Current
FWHM	Full Width at Half Maximum
HCL	Hollow Cathode Lamp
LED	Light Emitting Diode
LD	Laser Diode
MOSFET	Metal Oxide Semiconductor Field-Effect Transistor
PZT	Piezoelectric Transducer
Qubit	Quantum bit
rf	Radio Frequency
UV	Ultra-Violet
UHV	Ultra High Vacuum
Yb	Ytterbium

CHAPTER 1: INTRODUCTION

From the beginning of my association with this project, one goal has become apparent: To demonstrate a simple and inexpensive technique to trap a useful ion species. Ytterbium (Yb) fits the description of a useful ion species for numerous reasons elaborated below. Simple and cheap are, of course, relative terms, but if using off-the-shelf products in their intended or in novel ways yields results comparable to those achieved with custom components, then it stands to reason that the simple and cheap system will be more useful than the custom one.

Surface Ion Traps

Trapped ions are a potential candidate for quantum information processing¹. Conventional linear ion traps, using an axial arrangement of four parallel rods, have been shown to exhibit the characteristics of an envisioned quantum processor, including the ability to prepare a suitable quantum state that has a long relative decoherence time² and the ability to move the ions between zones (such as processing, memory, and cooling zones) using segmented control electrodes and T junctions.³ However, these macroscopic 3-dimensional traps, though feasible in isolated configurations, become quite complicated in any envisioned processing array. Moreover, the speed of quantum bit (qubit) rotations theoretically increases with decreased trap size, and these traps are difficult to miniaturize.

In contrast, a planar radio frequency (rf) Paul trap, where the electrodes all reside on a planar surface, has been demonstrated. Like a conventional linear trap, a surface trap exhibits the necessary control features, but has the added advantage of easy downward scaling in trap size as well as upward scaling in an array of traps and junctions to form a processor. Additionally, surface traps allow the trap position to be raised or lowered electrically. These traits, combined with an ability to fabricate such surface traps using

¹ J. Chiaverini, R. B. Blakestad, J. Britton, J.D. Jost, C. Langer, D. Liebfried, R. Ozeri, and D.J. Wineland, *Quantum Information and Communication*, **5**, 419-439, (2005).

² D. P. DiVinzenco, *Fortschr. Phys.* **48**, 771 (2000).

³ S. Seidelin, J. Chiaverini, R. Reichle, J. J. Bollinger, D. Liebfried, J. Britton, J. H. Wesenberg, R. B. Blakestad, R. J. Epstein, D. B. Hume, J. D. Jost, C. Langer, R. Ozeri, and D. J. Wineland, *quant-ph/0601173*.

commercially available printed circuit board materials and techniques, offer a tantalizingly simple and cost-effective technique to pursue quantum information processing.

Why Ytterbium?

Yb⁺ is a suitable candidate for trapping for numerous reasons. First of all, it has ground state transitions in both its neutral atom and singly ionized forms that are accessible (399.8 nm and 369.5 nm, respectively) by commercially available blue laser diodes. See Figure 1.

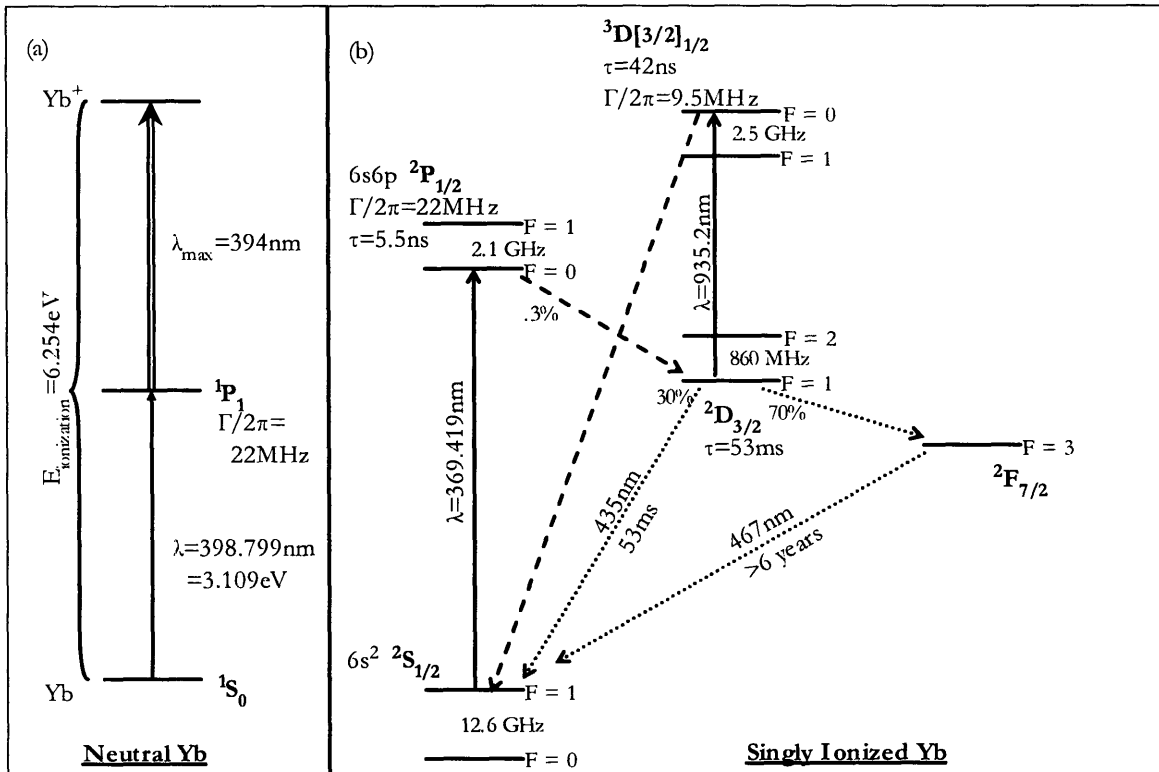


Figure 1 Relevant energy level diagram of Ytterbium (a) Ground state excitation and ionization energies. (b) Our excitation scheme relies on optically pumping Yb at 369.4nm and repumping via laser light at 935.2nm to avoid spontaneous decay to the long-lived ²F_{7/2} state. Potential applications as an optical frequency standard are indicated on the 435nm and 467nm transitions. Quantum computation schemes focus on the 435 transition or the 12.6GHz ground state hyperfine splitting.

It has a large hyperfine splitting (12.6 GHz) and a spontaneous decay ratio of P-S (369.5 nm) versus P-D (2438 nm) of 290 to 1.⁴ Furthermore, after excitation to the P-state by 399nm light, a neutral Yb is easily photoionized by light below 394nm, which can be

⁴ J. Yoda, and K. Sugiyama, J. Mod. Optics, **39**, 403-409 (1992).

provided by a simple ultra-violet (UV) light emitting diode (LED).⁵ The excitation of neutral Yb is isotope selective based on the resonance of the incident light, and photoionization avoids the addition of significant momentum and heating as well as the stray ionization and charging of nearby trap elements (control electrodes, chamber walls, etc.) that are common features of the alternative, electron impact ionization.⁶ ^{171}Yb , which is reasonably abundant in a natural sample (14.3%), is also especially attractive for use as a qubit because it is a spin-1/2 system (See Table 1), and it has a large hyperfine splitting of the ground state (12.6 GHz) and it is separated by almost 500MHz from the next nearest abundant isotope.⁷

Isotope	Mass [amu]	Abundance	Nuclear Spin	Mag Moment	Rel. Isotope Shift [MHz]
^{168}Yb	167.933894	0.13%	0		1887
^{170}Yb	169.934759	3.05%	0		1192
^{171}Yb	170.936323	14.3%	1/2	+0.4919	1153
^{172}Yb	171.936378	21.9%	0		533
^{173}Yb	172.938208	16.1%	5/2	-0.6776	-253
^{174}Yb	173.938859	31.8%	0		0
^{176}Yb	175.942564	12.7%	0		-509

Table 1: Relative Abundance of Ytterbium Isotopes.⁸

Singly ionized Ytterbium can be laser cooled in its ground state by the application of light at 369.4nm, which is accessible by commercially available UV laser diodes. The $^2\text{P}_{1/2}$ excited state spontaneously decays with a lifetime of 5.5ns and returns predominantly to the $^2\text{S}_{1/2}$ ground state. About 0.3% of the time, the excited state decays to the $^2\text{D}_{3/2}$ state, which is relatively long-lived with a lifetime of 53ms. During this time, the ion can be excited with

⁵ R.B. Warrington, P. T. H. Fisk, M. J. Wouters, M. A. Lawn, J. S. Thorn, S. Quigg, A. Gajaweera, and S. J. Park, Frequency Control Symposium and Exposition, 2005. Proceedings of the 2005 IEEE International, 231-234 (2005).

⁶ C. Balzer, A. Braun, T. Hannemann, C. Paape, M. Ettler, W. Neuhauser, and C. Wunderlich, quant-ph/0602044.

⁷ D. Das, S. Barthwal, A. Banerjee, and V. Natarajan. Phys. Rev. A **72** 032506 (2005).

⁸ Basic Atomic Spectroscopic Data, <http://physics.nist.gov/PhysRefData/Handbook/Tables/ytterbiumtable1.htm>, Aug 2005. Accessed April 22, 2006.

light at 935.2nm, driving a transition to the $^3D[3/2]_{3/2}$ state, which spontaneously decays in approximately 42ns, returning the ion to its ground state.⁹ The application of the 935nm “repumper” laser is necessary to avoid the effective loss of the ion by decay to the metastable state $^2F_{7/2}$, which has a lifetime on the order of a few years.¹⁰

⁹ A. S. Bell, P. Gill, H. A. Klein, A. P. Levick, C. Tamm, and D. Schnier. *Phys. Rev. A* **44** R20 (1991).

¹⁰ M. Roberts, P. Taylor, G. P. Barwood, W. R. C. Rowley, and P. Gill, *Phys. Rev. A* **62** 020501 (2000).

CHAPTER 2: EXPERIMENTAL SET-UP

Laser System

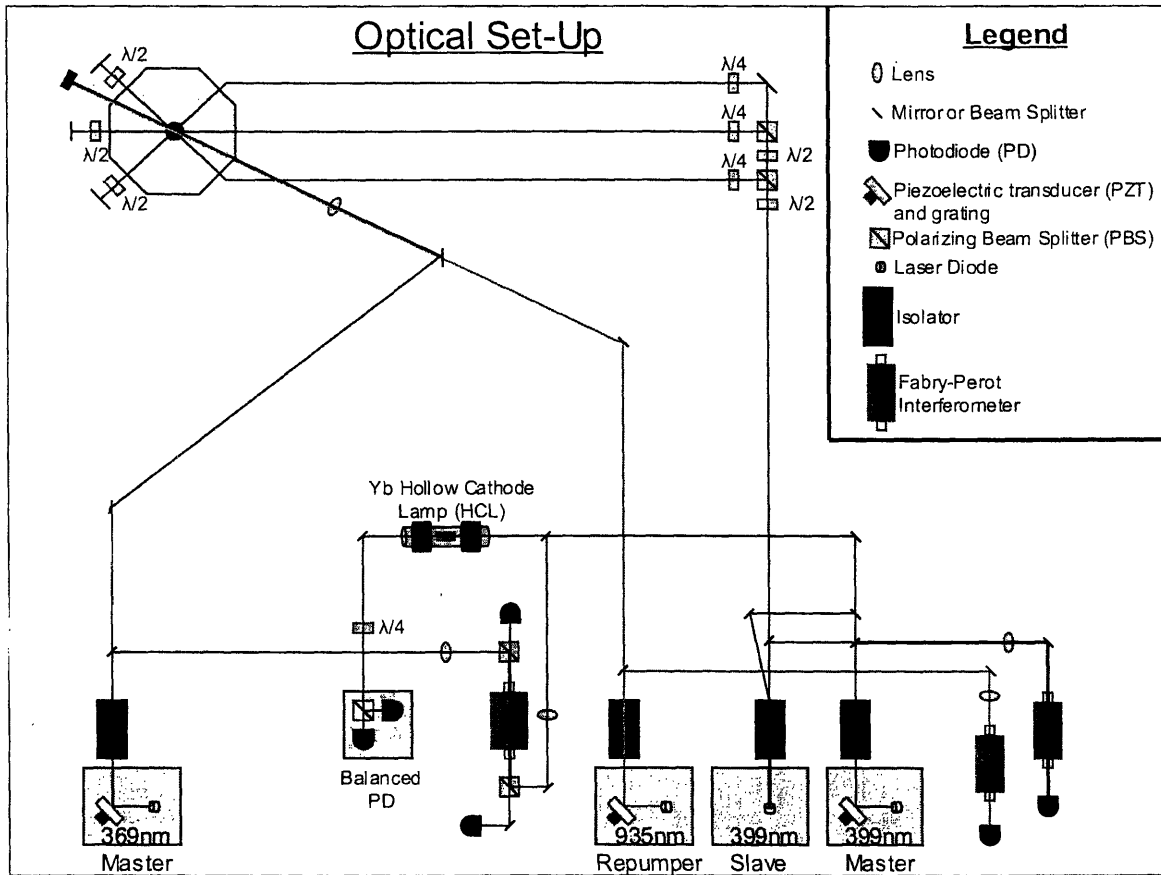


Figure 2 Experiment's Optical Set-Up Essential elements of the optical system are depicted, but additional steering mirrors, beam elevators, etc. are omitted for clarity.

Our base laser, the 399nm master, is an external cavity diode laser (ECDL) using a Nichia NDHV310ACAE1 laser diode. The laser diode is mounted in a temperature-stabilized base along with a collimation lens. The ECDL is operated in the Littrow configuration, where the laser grating's first order diffraction ($m=-1$) is fed back into the laser diode and the reflected beam becomes the laser's output.¹¹ The grating is mounted on a piezoelectric transducer (PZT), which expands and contracts depending on the voltage applied to it. The frequency of the laser output is dependent on temperature, PZT control of the grating, and diode current. Normally, we stabilize the temperature and use feedback

¹¹ C.J. Hawthorn, K.P. Weber, and R.E. Scholten, Rev. Sci. Inst., **72**, 4477 (2001).

to the PZT to control slow changes (10's of Hz) and adjustment of the laser current to control fast changes.

Immediately upon exiting the laser, we use an optical isolator to prevent any reflected beams from returning to the laser diode and affecting its frequency stability or even damaging the device. The isolators, when properly optimized, provide more than 70% transmission in the forward direction and more than 30 decibels of extinction in the reverse direction. These work by having an input polarizer, followed by a Faraday rotator, where in the presence of a longitudinal magnetic field, the beam polarization rotates in the same direction with respect to the magnetic field regardless of the beam's propagation direction. The Faraday rotator is followed by another polarizer. In the forward direction, the polarization, aligned with the first polarizer, rotates in the Faraday element and exits through the aligned second polarizer. In the reverse direction, the polarization exiting the Faraday rotator is at an angle of $\pi/2$ to the second polarizer and is extinguished.¹²

In typical operation, we get approximately 2.8 mW of power from the 399nm master laser after the isolator, which is split and used in four ways: to frequency lock the master laser (0.8mW), to provide beam diagnostics via a Fabry-Perot Interferometer (FPI) (0.4mW), to injection lock the 399nm slave laser (1.2 mW) and to lock a high finesse Zerodur FPI to use as a reference for the 369nm laser (0.4mW).

The 399nm slave laser consists solely of a laser diode and collimator in a temperature-stabilized mount. There is no grating; rather, light from the master laser, provided by a pick-off of the 399nm master beam, is injected back into the slave laser via the ejection facet of the downstream polarizer on the slave isolator. This light passes into the slave diode and when aligned and strong enough, causes lasing which is phase-locked to the master laser. The output of the slave laser after isolator is 12mW, of which 0.8mW is coupled into the diagnostic FPI. The remainder of the slave power is used in the magneto-optical trap.

¹² Orzaio Svelto, Principles of Lasers, trans. David C. Hanna (New York: Plenum Press, 1998), 288-289.

Laser Lock

The 399nm master laser is frequency locked to an external atomic reference using the Dichroic Atomic Vapor Laser Lock (DAVLL) technique.¹³ The atomic reference is provided by a commercially available Hollow Cathode Lamp (HCL), available from Hamamatsu (Model: L2783). The HCL consists of a transparent glass tube with a Yb cathode and an anode and a helium buffer gas, which when subjected to a high voltage ($\sim 135\text{V}$ in typical operation for our experiment), create a discharge plasma of Yb. When the master laser light, linearly polarized by the optical isolator, passes through the Yb vapor, it produces a Doppler-broadened absorption line (see Figure 3). In the presence of a magnetic field collinear with the laser, the absorption signal is Zeeman split. The linear polarization is equivalent to a combination of circularly polarized light (σ^+ and σ^-) with equal amplitudes. The circularly polarized light is preferentially absorbed by the Zeeman sub-levels (circular dichroism), leading to two separate absorption profiles. Upon passing through a quarter-wave plate, the two circular polarizations are resolved into orthogonal linear polarizations and these are split and sent to two photodiodes by a polarizing beam splitter (PBS)¹⁴, as in Figure 2. These two absorption profiles can be subtracted, leading to a locking signal which passes through zero at the central lock frequency.

¹³ K. L. Corvin, Z. T. Lu, C. F. Hand, R. J. Epstein, C. E. Wieman, *Appl. Opt.* **37**, 3295 (1998).

¹⁴ V. Yashchuk, D. Budker, J. Davis, *Rev. Sci. Instr.* **71** 341 (2000).

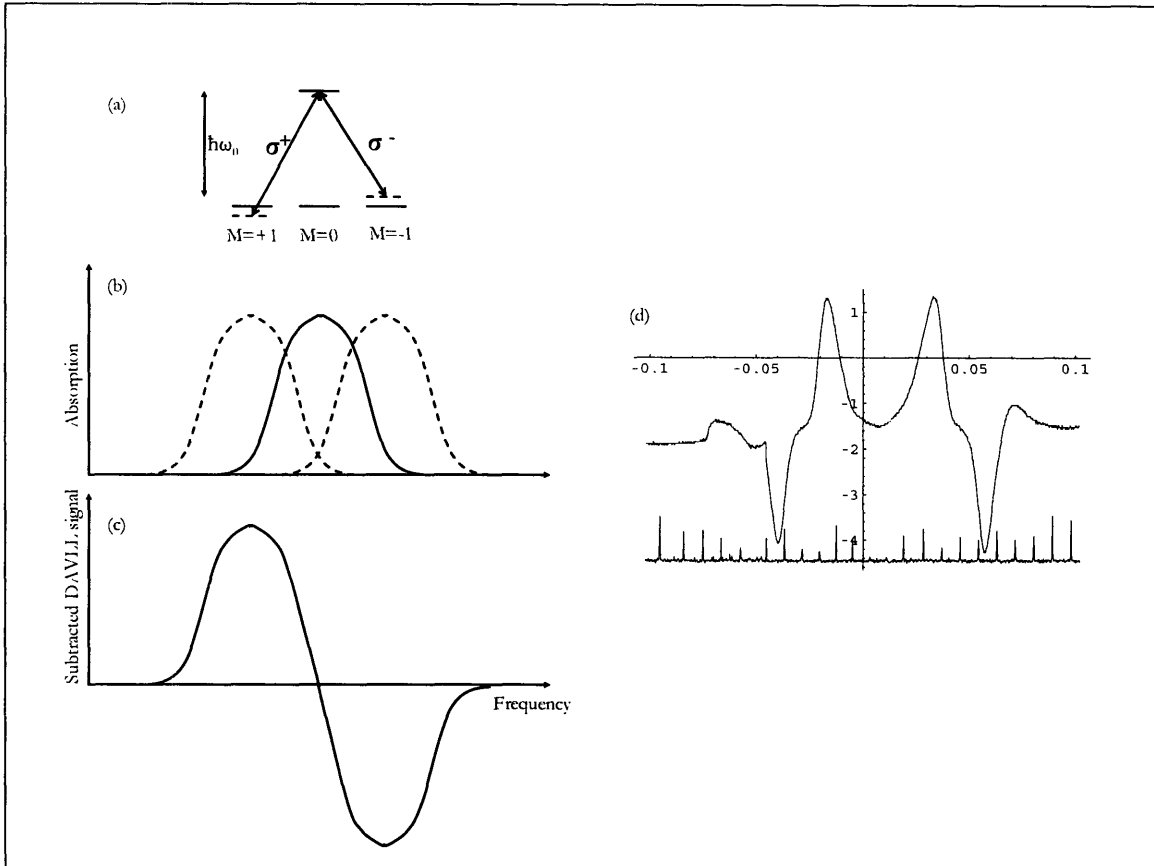


Figure 3 Dichroic Atomic Vapor Laser Lock (a) Zeeman splitting of resonant frequency ω_0 experienced by circularly polarized (σ^+ and σ^-) light. (b) Doppler-broadened resonant absorption profile in solid line; Zeeman shifted peaks in dashed line. (c) Electronic subtraction of the two absorption features results in a wide frequency range with a steep error-signal slope. (d) A representative DAVLL trace from our lock (top) and Fabry-Perot fringe spacing at 1GHz (bottom).

In our set-up, the HCL is surrounded by two sets of ring-shaped, cylindrical rare-earth magnets. These provide a magnetic field which is roughly constant and axial (as in a solenoid) in the atomic vapor region. The Zeeman splitting is proportional to the magnetic field applied, $E_B = 2g\mu_B B$, where g is the Lande factor and μ_B is the Bohr magneton. The frequency splitting ($2g\mu_B B/\hbar$) between the absorption peaks is proportional to the applied magnetic field, and the magnetic field used is ultimately a trade-off between a large recapture range, represented by a large frequency splitting, and a strong error signal, represented by the steepness of the zero-crossing slope of the subtracted signal.

Our DAVLL apparatus was optimized with a magnetic field strength of approximately 50 Gauss in the atomic vapor region, although some shielding of the magnetic field is likely by the lamp itself.¹⁵ A representative lock trace is in figure 3(d).

Isotope Selectivity

The HCL and the chamber oven contain all isotopes of Yb (See Figure 4). Sweeping the laser lock through the absorption peak results in the trapping laser beams coming into resonance with the isotopes in the vapor. Each isotope (that is present in sufficient quantity) can then be trapped in the MOT. We have routinely captured ¹⁷¹Yb, ¹⁷²Yb, ¹⁷³Yb, and ¹⁷⁴Yb in our MOT.

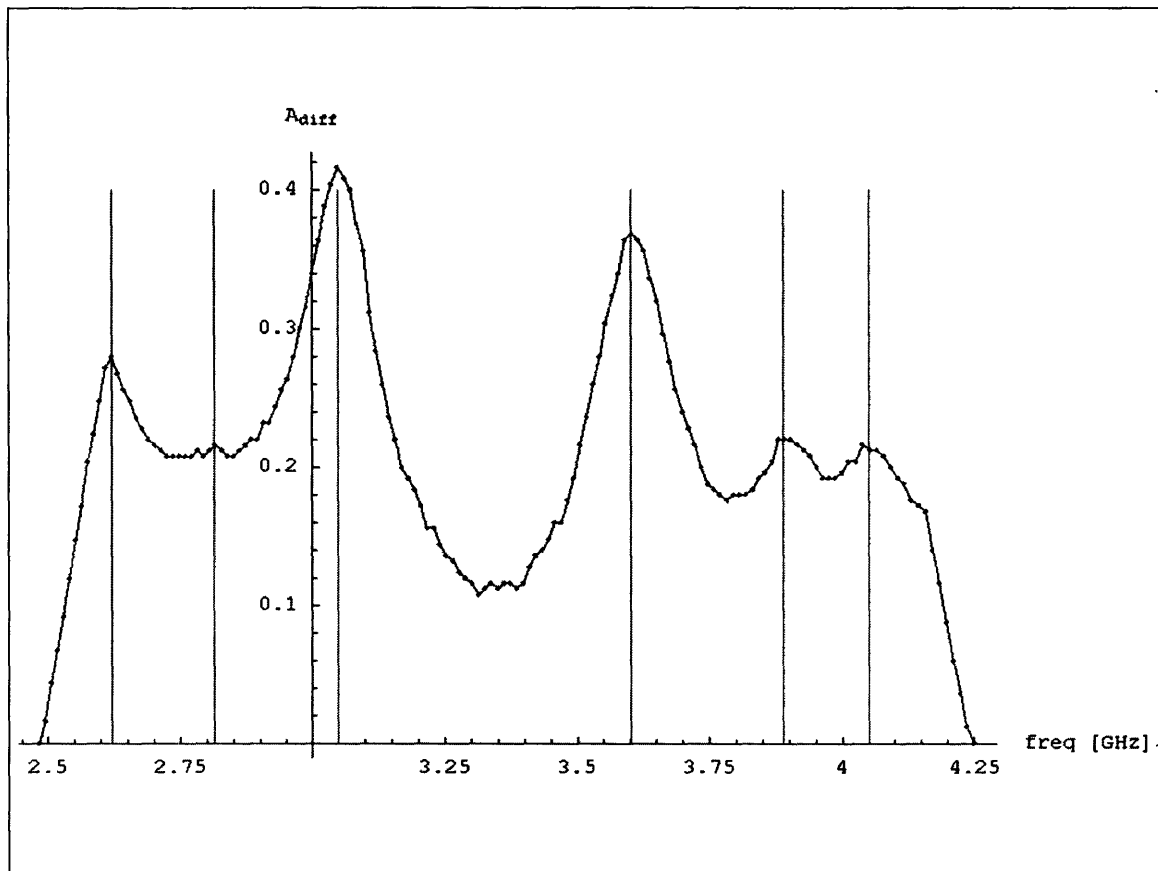


Figure 4 Absorption Spectra experienced in Yb HCL Conducting saturated absorption spectroscopy, we observed isotope peaks from left to right: ¹⁷⁶Yb, ¹⁷³Yb, ¹⁷⁴Yb, ¹⁷²Yb, ¹⁷¹Yb_{|=3/2}, ¹⁷¹Yb_{|=1/2} with detunings of -428.2, -233.2, 0, 554.2, 841.8, 1001.8 MHz, respectively.

¹⁵ J. I. Kim, C. Y. Park, J. Y. Yeom, E. B. Kim, T. H. Yoon, Opt. Lett. **28** 245 (2003).

Trapping Chamber

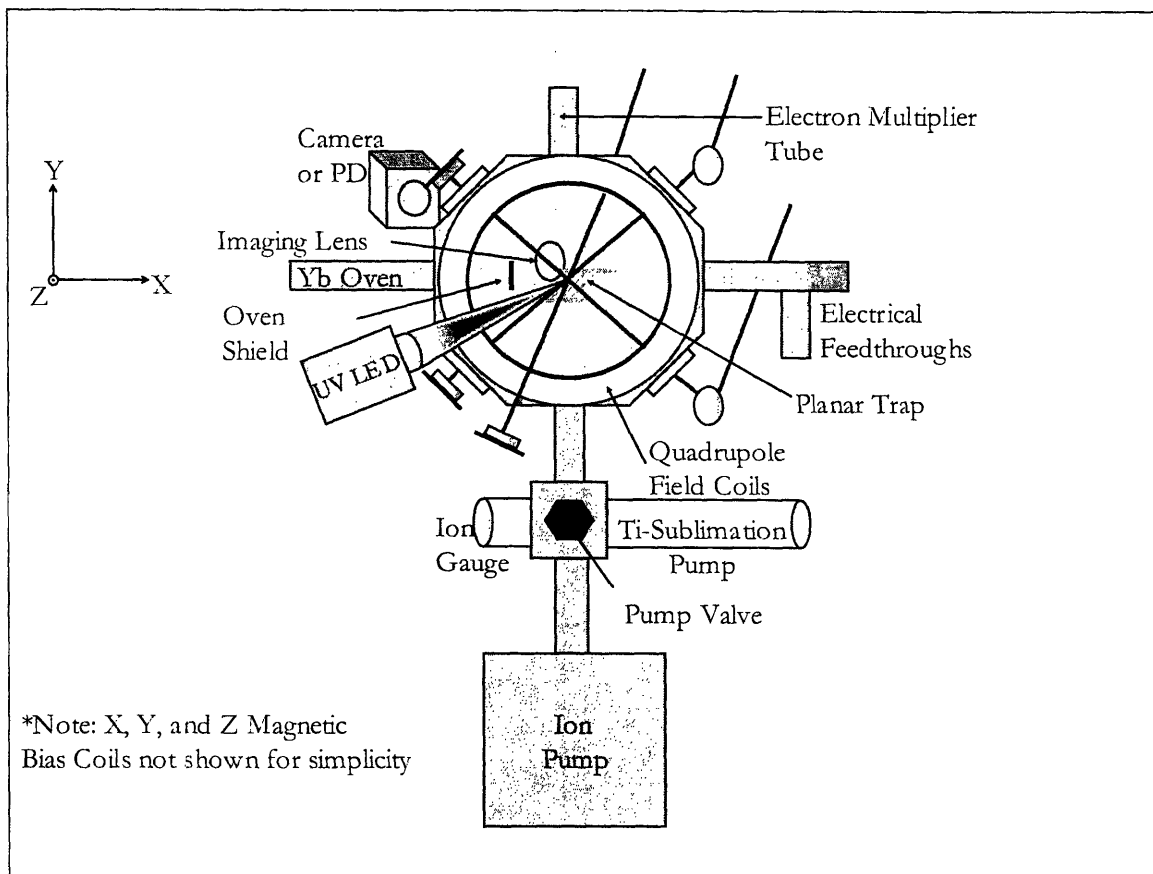


Figure 5 Trapping chamber Essential elements of the trapping chamber and vacuum system are indicated.

Our atomic vapor source is a thermal oven, consisting of a few Ytterbium metal flakes surrounded by a tantalum foil shield with a pinhole for emission. This Yb oven is held on an electrical feedthrough in a recessed arm of the vacuum chamber. During early use, this configuration resulted in significant Yb deposition on the walls and optical windows on the side of the chamber opposite the oven. To limit the adverse effect of this deposition, we installed a copper baffle to shield the trap electrodes from the oven and recessed the oven 7cm from the chamber center.

The trapping chamber consists of a spherical octagon (Kimball Physics, Inc., Model: MCF450-SO20008-A), made of UHV stainless steel, with two 4 1/2" main windows and eight 1-1/3" side viewports. All windows have anti-reflective coating for 369nm and 399nm (<.5% reflectivity). The Yb oven is mounted on one side port, with the electrical feedthroughs mounted opposite. The trap chip lies centered but 3mm below the geometric

center of the chamber, and a small copper shield is between the oven and the trap chip to prevent Yb coating and possible shorting of the trapping electrodes. An aspherical lens of focal length 1.7cm lies at one corner of the trap to provide external imaging of the trapping region with a camera or photodiode. A Burle Magnetron 5901 Channeltron electron multiplier is installed in the chamber port above the trap. Below the chamber, there is a joint which provides access to a nude ion gauge, a Titanium sublimation pump, and an ion pump. The remaining windows are used for optical beam access for the cooling lasers or ionizing LED.

Magneto-Optical Trapping

We accomplish trapping of our neutral atoms in a Magneto-Optical Trap (MOT). The trapping mechanism of a MOT can best be understood in one-dimension, (see Figure 6(a)). Atoms with a ground state angular momentum of $J_g=0$ and an excited state angular momentum of $J_e=1$ experience a shift to three Zeeman sub-levels in the presence of a magnetic field, $\mathbf{B}(z)=B_z z \mathbf{e}_z$. The magnetic field is a linear, but inhomogeneous field, which is zero at the origin, such as that provided by two current loops in an anti-Helmholtz configuration. The excited state energy for each of the $m_j=\pm 1$ sub-levels is $E_e^{\pm 1} = \hbar\omega_0 \pm \mu B(z)$, where ω_0 is the atomic transition frequency in the absence of a magnetic field, and μ is the magnetic moment in the magnetic field direction.¹⁶

¹⁶ V.S. Letokhov, "Electromagnetic Trapping of Cold Atoms: An Overview," in Trapped Particles and Fundamental Physics, ed. S.N. Atutov, R. Calabrese, and L. Moi (Dordrecht, The Netherlands: Kluwer, 2002), 29-32.

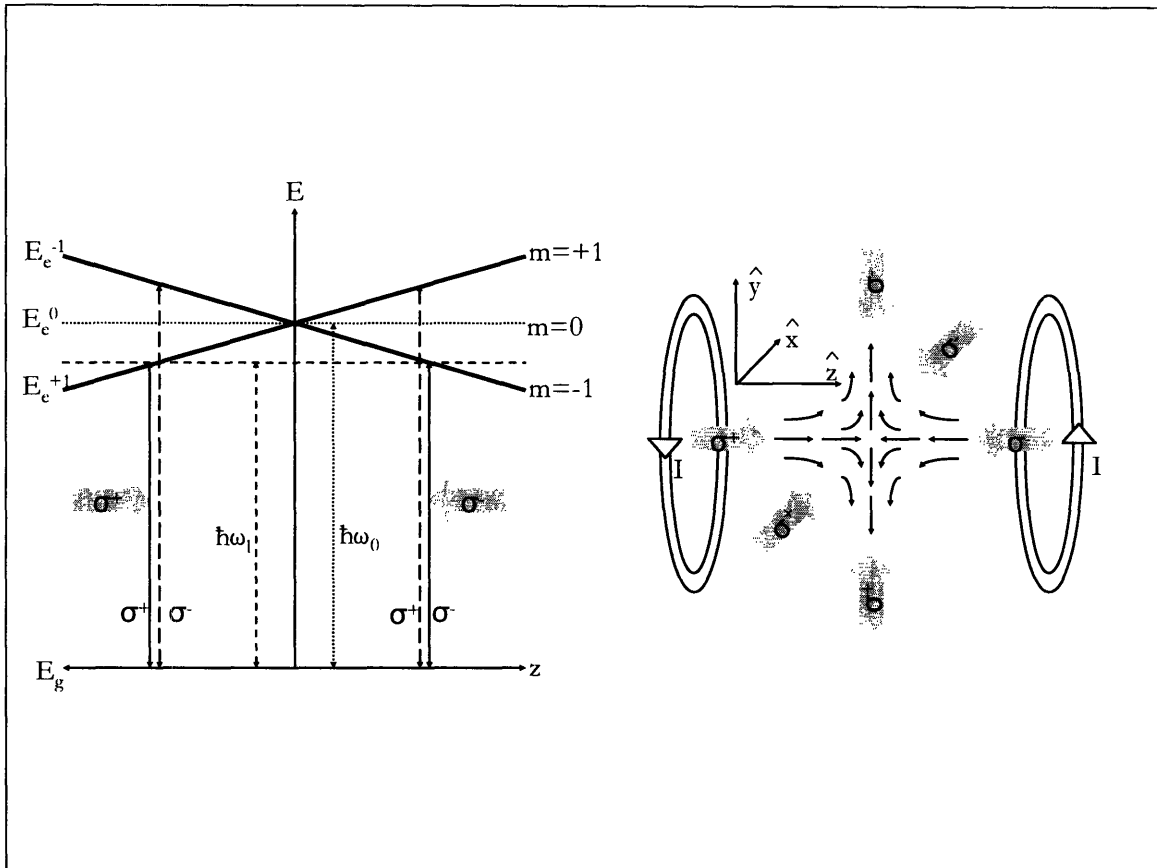


Figure 6 Magneto-Optical Trap (a) 1-D: In the presence of an inhomogeneous magnetic field and a red-detuned laser ($\omega_1 < \omega_0$), circularly polarized light preferentially absorbs based on which side of the magnetic field origin it is located on, and then it re-radiates in a random direction, thereby imparting a net restorative force. (b) 3-D trapping in an appropriate magnetic field is a simple extension of the 1-D case.

Assuming a red-shifted laser frequency, ω_1 , such that $\omega_1 < \omega_0$, and light that is left and right circularly polarized (σ^+ , σ^-) propagating in the $\pm z$ direction, atoms to the right (left) of the origin will preferentially absorb σ^- (σ^+) polarized light, since it is closer to resonance. The atom reradiates this energy into a full 360° , thereby imparting a net radiation pressure force which is restorative (ie pushes the atom back toward the origin). This results in a potential well that traps atoms at the origin. This radiation pressure acts to restore the atom in position space in the same way that velocity damping (as in optical molasses) via the Doppler effect acts in velocity space.¹⁷

¹⁷ Harold J. Metcalf, and Peter van der Straten, *Laser Cooling and Trapping*, (New York: Springer, 1999), 87-90, 156-158.

This configuration can be easily extended to three dimensions, as illustrated in Figure 6(b), with three counter-propagating beams where the atoms are confined in each direction independently as previously described.¹⁸

Ionization

We photo-ionize from the excited 1P_1 state of neutral Yb (see Figure 1(a)) using a commercially available Nichia NCCU001E High Power Chip Type UV LED. This LED provides approximately 85mW of optical output power in a broad spectrum (± 15 nm FWHM) at a peak of 385nm. See Figure 7. Light at 394nm or less is sufficient to overcome the binding energy of the outermost electron and create singly-ionized Yb.

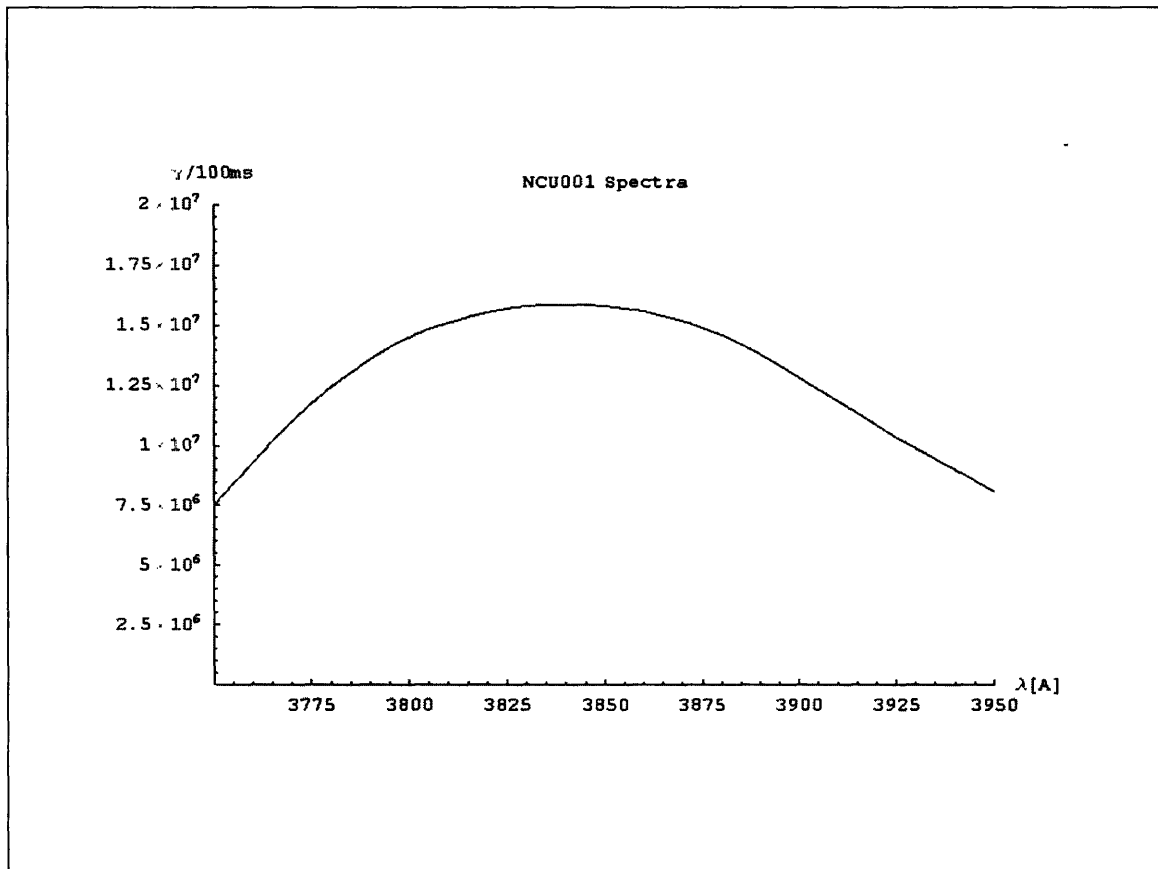


Figure 7 Emission Spectra of Ionizing LED Focused light from the broadband UV LED provides ionization energies below 394nm.

¹⁸ E.L. Raab, M. Prentiss, A. Cable, S. Chu, and D. E. Pritchard, Phys. Rev. Lett. **59**, 2631 (1987).

The output of the UV LED is focused using a lens system such that the image of the LED is slightly larger than the MOT size about 8cm in front of the forward lens. This configuration allows us to concentrate the ionizing photons from the UV LED into the MOT region and easily maximize the ion signal.

Condition	Oven On	MOT Present	Main MOT coils On	399 Laser On	Bias Coils On	Count Rate[kHz]	
						UV Off	UV On
Background Only	N	N	N	N	N	<1	n/a
Atomic Vapor Only	Y	N	Y	N	N	3.1	6.3
Optical Molasses	Y	N	Y	Y	N	3.9	118
MOT	Y	Y	Y	Y	Y	4.9	227

Table 2 Photoionization Levels Photo-ionization rates depend heavily on the presence of the MOT and the UV LED. Counts are taken with a voltage of -1.9kV on the ion detector.

Ions in the trapping chamber were detected using a Burle 5901 Magnum Channeltron Electron Multiplier™ (CEM). A CEM operates analogously to a photomultiplier tube.¹⁹ For positive ions, a large negative voltage (for us, -1.9 to -2.0kV) is applied near the detecting end of a tube, causing positive ions to strike the channel walls, producing 2-3 additional electrons which move toward the lower-voltage end of the detector, striking the wall again and producing additional electrons. Typical total gain is on the order of 10^7 . This current flows across a resistor to ground and generates a voltage relative to ground. Thus, each ion that arrives at the detector creates a voltage pulse. We filter the signal with a 30MHz low-pass filter, and then we amplify these voltage pulses to the 10's of milli-volts range for detection.

Ion Trapping

The principles of an rf-Paul trap for ions are best understood in a perfect quadrupole geometry.²⁰ A quadrupole geometry depends on the square of the distance from the quadrupole origin. The potential in a quadrupole field in three-dimensions is:

¹⁹ Burle Technologies, Inc. "Channeltron Electron Multiplier Handbook for Mass Spectrometry Applications."

²⁰ Pradip K. Ghosh, *Ion Traps*, (Oxford: Clarendon Press, 1995), 7-20.

$$\Phi = \frac{\Phi_0}{r_0^2} (\alpha x^2 + \beta y^2 + \gamma z^2) \quad [1]$$

where Φ is the electric potential, α , β , and γ are the scaling factors on the Cartesian coordinates x , y , and z , and r_0 is the radial distance and defines the required quadrupole field. Laplace's equation dictates that:

$$\nabla^2 \Phi = \frac{\Phi_0}{r_0^2} (2\alpha + 2\beta + 2\gamma) = 0 \quad [2]$$

There are an infinite combination of α , β , and γ that satisfy Equation 2, but the simplest way is the two-dimensional field for $\alpha = -\beta = 1$, and $\gamma = 0$ ²¹

$$\Phi = \frac{\Phi_0}{r_0^2} (x^2 - y^2) \quad [3]$$

The two-dimensional case is physically a set of four hyperbolically-shaped rods, as shown in Figure 8. An alternating rf-potential is applied to these electrodes of the form

$$\Phi_0 = \pm(U - V \cos \Omega t) \quad [4]$$

where U is a DC "offset" voltage and $V \cos \Omega t$ is an rf voltage of frequency Ω . The resulting potential is

$$\Phi(x, y, t) = (U - V \cos \Omega t) \frac{(x^2 - y^2)}{r_0^2} \quad [5]$$

²¹ W. Paul, "Electromagnetic Traps for Charged and Neutral Particles," Nobel Lecture, 1989.

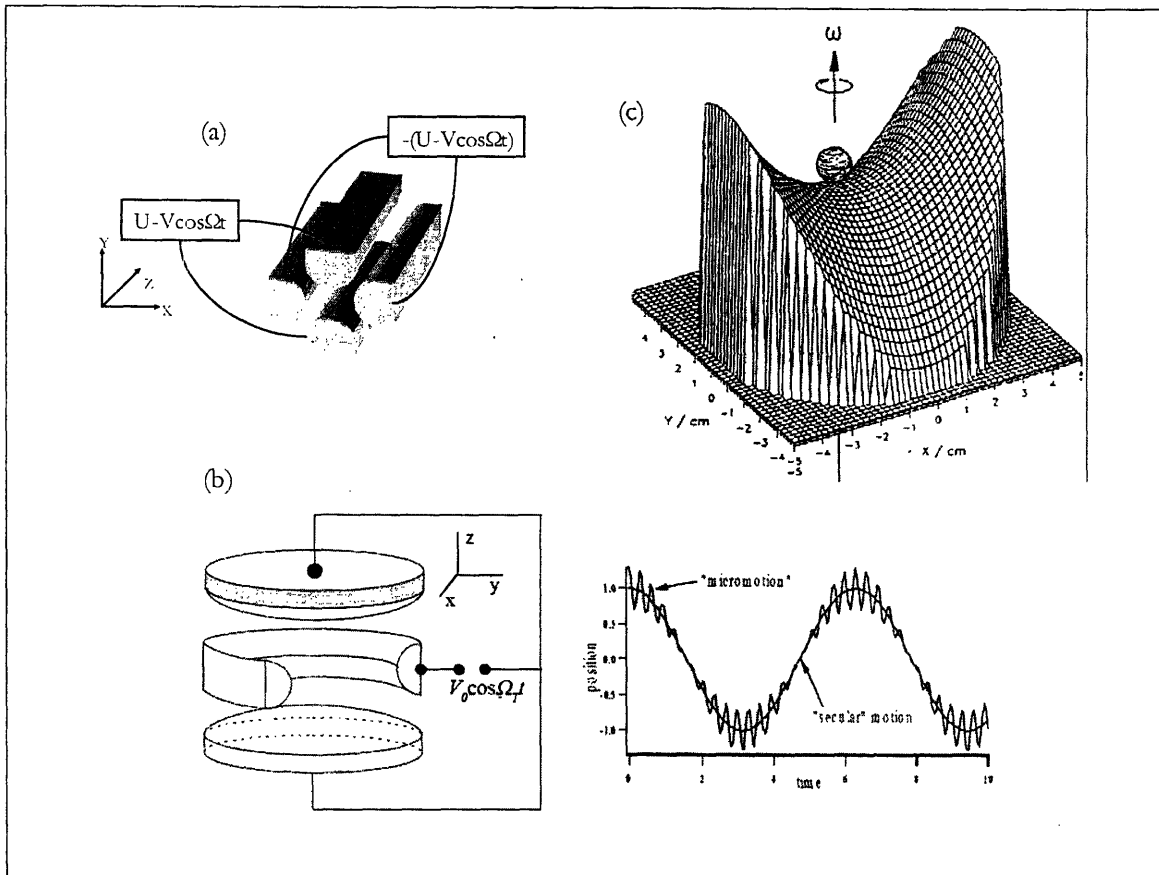


Figure 8 Radio Frequency Paul Trap (a) Out-of-phase alternating radio frequency electrodes provide trapping in 2-dimensions. (b) A three-dimensional trap is illustrated along with “micromotion” and “secular” motion.²² (c) A physical model presented by Paul himself illustrates the concept behind the rf trap using a small ball in an unstable saddle which is confined when the saddle is rotated at an appropriate angular frequency, ω .

The force on an ion of mass m and charge e is²³

$$\vec{F} = m\vec{A} = -e\nabla\Phi \quad [6]$$

resulting in ion motion

$$\ddot{x} + \frac{e}{mr_0^2}(U - V\cos\Omega t)x = 0 \quad \text{and} \quad \ddot{y} - \frac{e}{mr_0^2}(U - V\cos\Omega t)y = 0 \quad [7]$$

To match the canonical form $(\frac{d^2 u}{d^2 \zeta} + (a - 2q\cos 2\zeta)u = 0)$ of the differential equation

known as the Mathieu equation, we can substitute

²² Course Handout, MIT 8.422, Problem Set 10, May 2005.

²³ John F. J. Todd, “Ion Trap Theory, Design, and Operation,” in Practical Aspects of Ion Trap Mass Spectrometry, ed. R. E. March and J.F.J. Todd (Boca Raton: CRC Press, 1995), 7-12.

$$a \equiv \frac{4eU}{mr_0^2\Omega^2} \quad q \equiv \frac{2eV}{mr_0^2\Omega^2} \quad \zeta \equiv \frac{\Omega t}{2} \quad [8]$$

to yield

$$\frac{d^2 x}{d^2 \zeta} + (a - 2q \cos 2\zeta)x = 0 \quad \text{and} \quad \frac{d^2 y}{d^2 \zeta} - (a - 2q \cos 2\zeta)y = 0 \quad [9]$$

The Mathieu equation has both stable and unstable solutions in the a - q parameter space. In the first stability region, q (known as the Mathieu parameter) can range up to 0.908.

In a three-dimensional quadrupole trap (the case of $\alpha=\beta=1$ and $\gamma=-2$ in Equation 2)

$$\Phi = \frac{\Phi_0}{r_0^2} (r^2 - 2z^2) \quad [10]$$

in which $r^2 \equiv x^2 + y^2$ represents the radial direction since the x - and y -equations are identical.

The equations of motion become:

$$\ddot{r} = \frac{-2e}{mr_0^2} \Phi_0 r \quad [11]$$

$$\ddot{z} = \frac{4e}{mr_0^2} \Phi_0 z \quad [12]$$

The parameter substitutions and Mathieu equations are thus

$$a_z = -2a_r = \frac{-8eU}{mr_0^2\Omega^2} \quad q_z = -2q_r = \frac{-4eV}{mr_0^2\Omega^2} \quad \zeta \equiv \frac{\Omega t}{2} \quad [13]$$

$$\frac{d^2 r}{d^2 \zeta} + (a_r - 2q_r \cos 2\zeta)r = 0 \quad \text{and} \quad \frac{d^2 z}{d^2 \zeta} - (a_z - 2q_z \cos 2\zeta)z = 0 \quad [14]$$

The total motion is composed of both faster, smaller oscillations at the rf-drive frequency Ω (the so-called “micro-motion”) and a larger, slower oscillation at the “secular” frequency, to be formally defined shortly. We will examine the total motion in the z -direction, and assume that the rf-offset (U) is zero for simplicity, so equation 12 becomes

$$\ddot{z}_{total} = \frac{4e}{mr_0^2} V \cos(\Omega t) z_{total} \quad [15]$$

Knowing $z_{total} = z_s + z_\mu$ and $\ddot{z}_{total} = \ddot{z}_s + \ddot{z}_\mu$, then

$$\ddot{z}_s + \ddot{z}_\mu = \frac{4e}{mr_0^2} V \cos(\Omega t) (z_s + z_\mu) \quad [16]$$

Because of the differences in scale, one can assume that $z_\mu \ll z_s$ and $\ddot{z}_\mu \gg \ddot{z}_s$ so that this simplifies to

$$\ddot{z}_\mu = \frac{4e}{mr_0^2} V \cos(\Omega t) z_s \quad [17]$$

Since the only time-dependence is in the cosine term, differentiation of the micro-motion allows the substitution $\ddot{z}_\mu = -\Omega^2 z_\mu$, yielding

$$z_\mu = -\frac{4e}{mr_0^2} V \cos(\Omega t) z_s \quad [18]$$

Substituting these last two equations back into Equation 16, shows that

$$\ddot{z}_s + \frac{4e}{mr_0^2} V \cos(\Omega t) z_s = \frac{4e}{mr_0^2} V \cos(\Omega t) \left(z_s - \frac{4e}{mr_0^2} V \cos(\Omega t) z_s \right) \quad [19]$$

Time-averaging over the micro-motion at Ω so that $\langle \cos \rangle = 0$ and $\langle \cos^2 \rangle = 1/2$ simplifies this to

$$\ddot{z}_s = \frac{-8e^2 V^2}{m^2 r_0^4 \Omega^2} z_s = -\omega_z^2 z_s \quad [20]$$

where we have defined $\omega_z \equiv \frac{2\sqrt{2}eV}{mr_0^2 \Omega}$ which also equals $\omega_z = \frac{q}{2\sqrt{2}} \Omega$ using the definition of q from Equation 13.

Our printed circuit board trap is illustrated in Figure 9. It consists of a commercially printed circuit on an rf-suitable substrate (Rogers 4350), with a ground and an rf-electrode, and three sets of smaller compensation electrodes.

We modeled the potentials surrounding these trapping electrodes using the Boundary Element Method (BEM). It uses an electrostatic Green's function to solve for a charge distribution on the electrodes which reproduces the potential specified on the electrodes. This charge distribution then determines the potential everywhere.

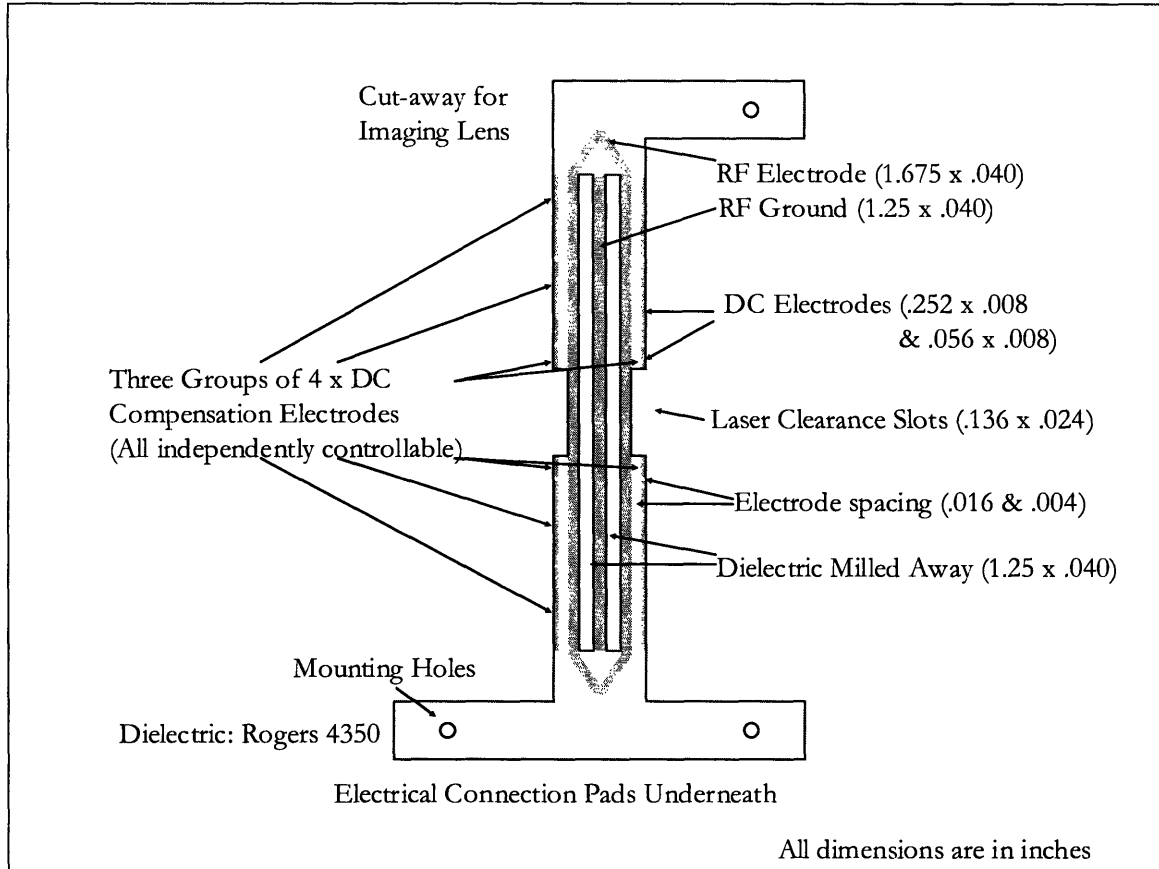


Figure 9 Planar Trap Design Trapping electrodes and compensation electrodes are as shown. The inner dielectric surface of the rf-electrodes is coated with conductor to minimize exposure of the trapping region to potentially charged dielectric.

The height of the trap above the rf-trapping electrodes can be varied by adjusting the ratio of the rf-amplitudes (rf electrode vs. rf ground) and their relative phase. Given the constraints of laser beam clearance through the viewports and through the laser clearance slots on the trapping chip, our MOT is approximately 3mm above the trap surface, and we operate the trap amplitudes 180° out-of-phase and at a ground-rf ratio of 0.6, as indicated in Figure 10.

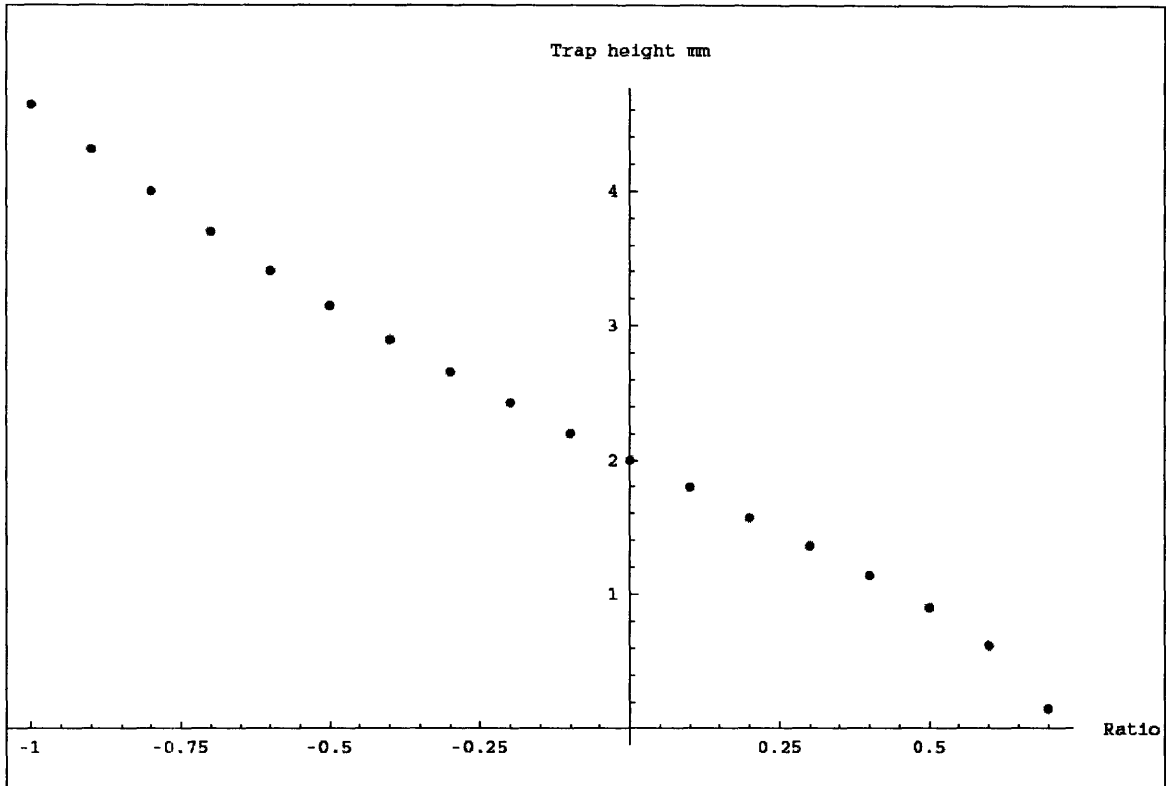


Figure 10 Trap center height calculated as a function of ground-rf electrode ratio. Positive ratio represent in-phase amplitudes, while negative ratios represent out-of-phase ratios. The trapping region, computed via BEM, extends approximately 1mm on either side of the center.

CHAPTER 3: RESULTS

Ion Detection

Detection of the ions produced from the MOT was a significant challenge. Initial indications that the UV LED was ionizing correctly was provided by a decreased fluorescence from the MOT when the UV LED was on, indicating that the MOT loss rate was increased. After adding an ion detector to the vacuum chamber, we confirmed this result as indicated in Table 2. Confirmation of ion trapping would be provided by this same ion detector.

We needed to know when to look for an ion signal from the trap. Initial tests indicated that the ions required about 5 μs to travel the approximately 10cm from the trapping region to the ion detector. To eliminate the possibility that stray electric fields near the trap could greatly influence this travel time to the detector, we applied a range of negative voltages to the offset electrodes on the trap. We found that the travel time is relatively insensitive to the offset voltages (total change of 1.4 μs), although as expected, with larger (negative) offset voltages the number of ions arriving at the detector decreased, presumably because an increasing number of the ions were being attracted to the offset electrodes rather than the ion detector. At about -170V, the voltage offset began to dominate the ion detector. We concluded that we would see ions 5.2 μs after the ion detector's high voltage turn-on. See Appendix B (Response Times).

DC Offset

With all the requisite trapping elements present (cold atom source in the MOT, photoionization via the UV LED, ion detector, and an rf potential applied to the trapping electrodes), we did not see any evidence of trapping after numerous attempts. We suspected a stray or residual electric field in the trap region. Using the control electrodes on the edge of the chip trap, we tried various offset voltages to eliminate or reduce the stray electric field. Offsetting the inner set of four electrodes to +18(2)V produced an ion signal at the detector which seemed to occur at the anticipated time after the detector turn-on, and responded to the relevant control elements (trapping fields, ion sources, etc.).

In subsequent trials, a negative DC offset of $-4.5 \pm 1\text{V}$ applied to the rf-electrodes produced an identical signal. This can be explained by the four inner electrodes having an

essentially dipole-like field at distances (like the trapping region) that are long compared to the distance between the electrodes and DC-ground (ie the trapping electrodes at .016”).

Trapping Ions

The scheme for measuring the ions in the trap was to keep the rf trapping voltages applied to the middle trap rods and the UV LED focused on the MOT for a load time, T_l . Then, we turned off the UV LED, but left on the rf voltages for a storage time, T_s . In some iterations, we would turn everything off for a dump time, T_d . Finally, we would turn on the ion detector for a 50 μ s time.

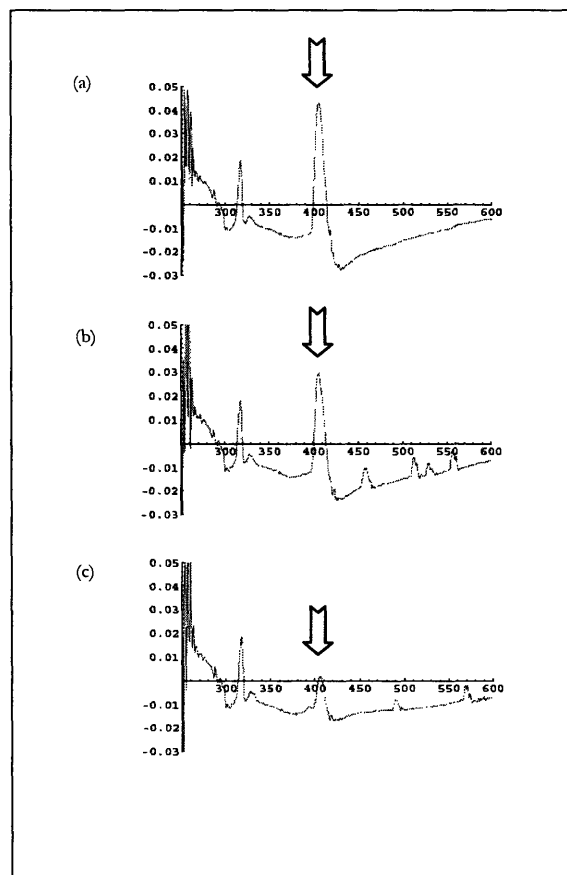


Figure 11 Trapping Ions Loading time: 200ms, Dumping time: 0ms, sequence of storage times: (a) 10ms, (b) 100ms, (c) 500ms. Ion signal is indicated by the arrow. Horizontal scale is in 10^{-8} sec (ie the trapping signal is at 4 μ s). The static initial spike and the peak at 3.25 μ s are noise from the high voltage turn-on.

The initial evidence of trapping is shown in Figure 11, where for an adequate loading time, the ions arriving at the detector show a downward trend for increased storage time. In Figure 12, the trap is turned off for an increasing “Dump Time,” which allows the trapped

ion cloud to begin to expand under their mutual repulsion. A small expansion of the cloud, representing a weaker trap, is shown in Figure 12(b), where the detected signal is broader and begins earlier. This is indicative of some of the ions starting closer to the trap and of the ion cloud starting from a spatially larger region.

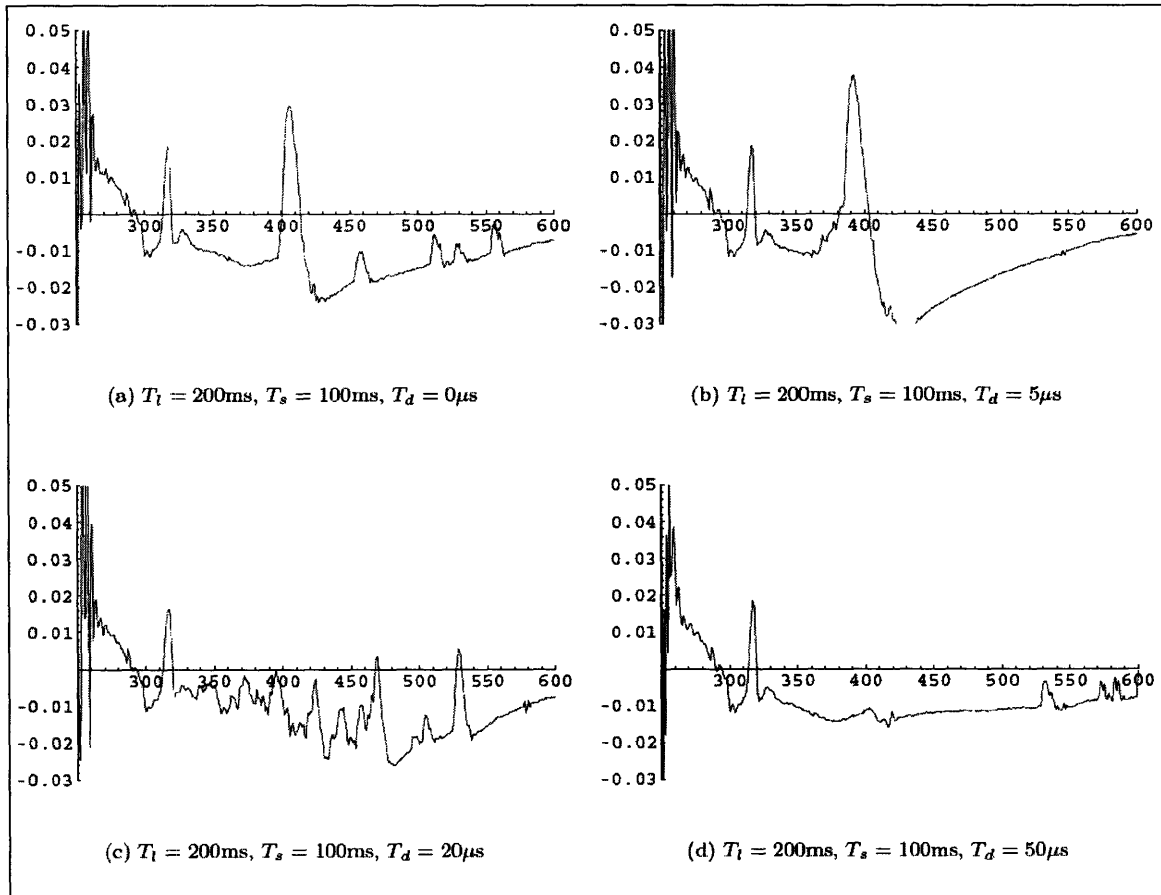


Figure 12 Dependence of trap on increasing “dump time.” Note the broadening of the ion’s arrival time at the detector in (b), followed by the arrival of widely-spaced ions in (c). (d) shows the complete loss of the released ions to the chamber.

This trend is amplified in a dumping time of $20\mu\text{s}$ as indicated in Figure 12(c). Here the ion cloud has expanded greatly and the ions are in the process of flying toward the trap chamber walls when the ion detector is turned on and gathers all the ions. The arrival of the ions is spread out over a $2\mu\text{s}$ time period and the detection signal shows characteristics of individual or small groups of ions arriving. Finally, by $50\mu\text{s}$, the ions have all flown to the grounded chamber walls, and no ions are detected.

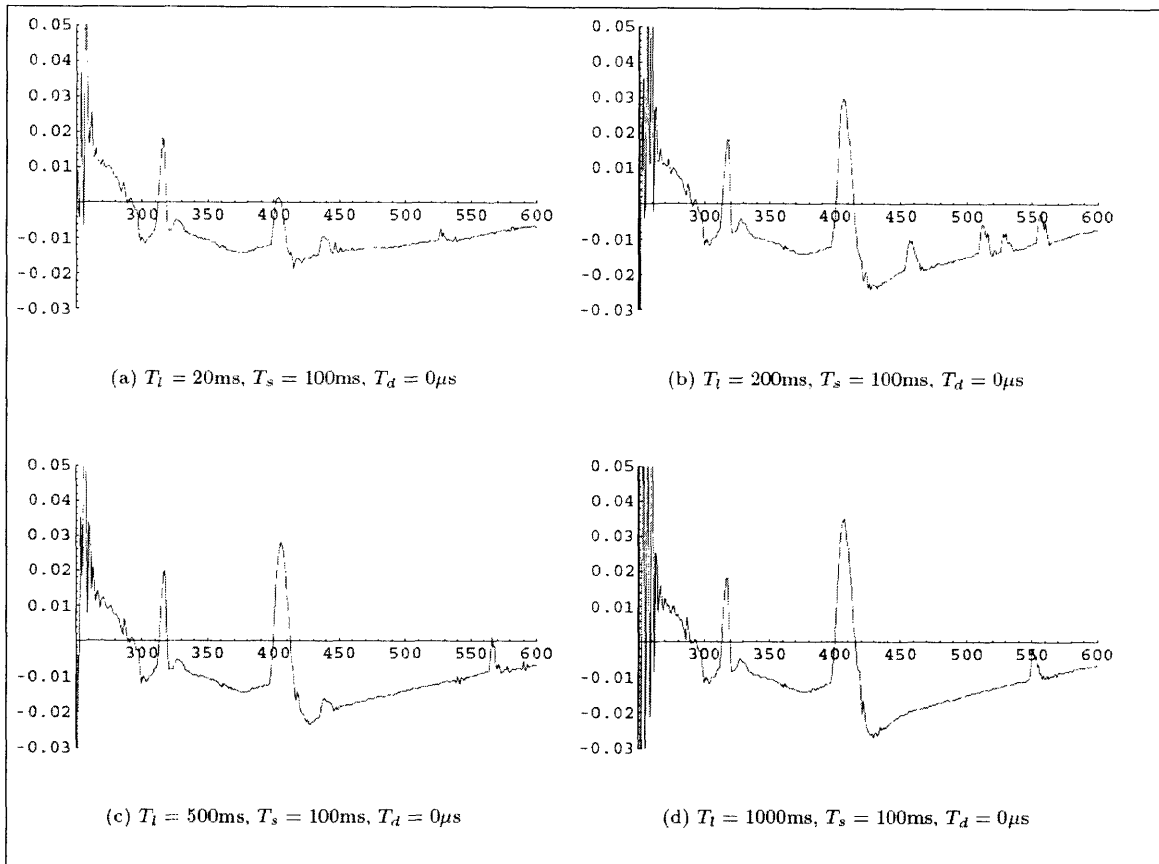


Figure 13 Dependence of Trap on Loading Time Increased loading times yield more trapped and detected ions (a)-(d).

We expected the trap to have a dependence on the loading time, as indicated in Figure 13. Increasing the amount of time the trap has to load increases the number of ions that can be detected. After a certain loading time, however, there is a balance between new ions being trapped and the loss of ions already trapped, indicating a fully-loaded ion trap. The loss of ions over time can be seen in Figure 14.

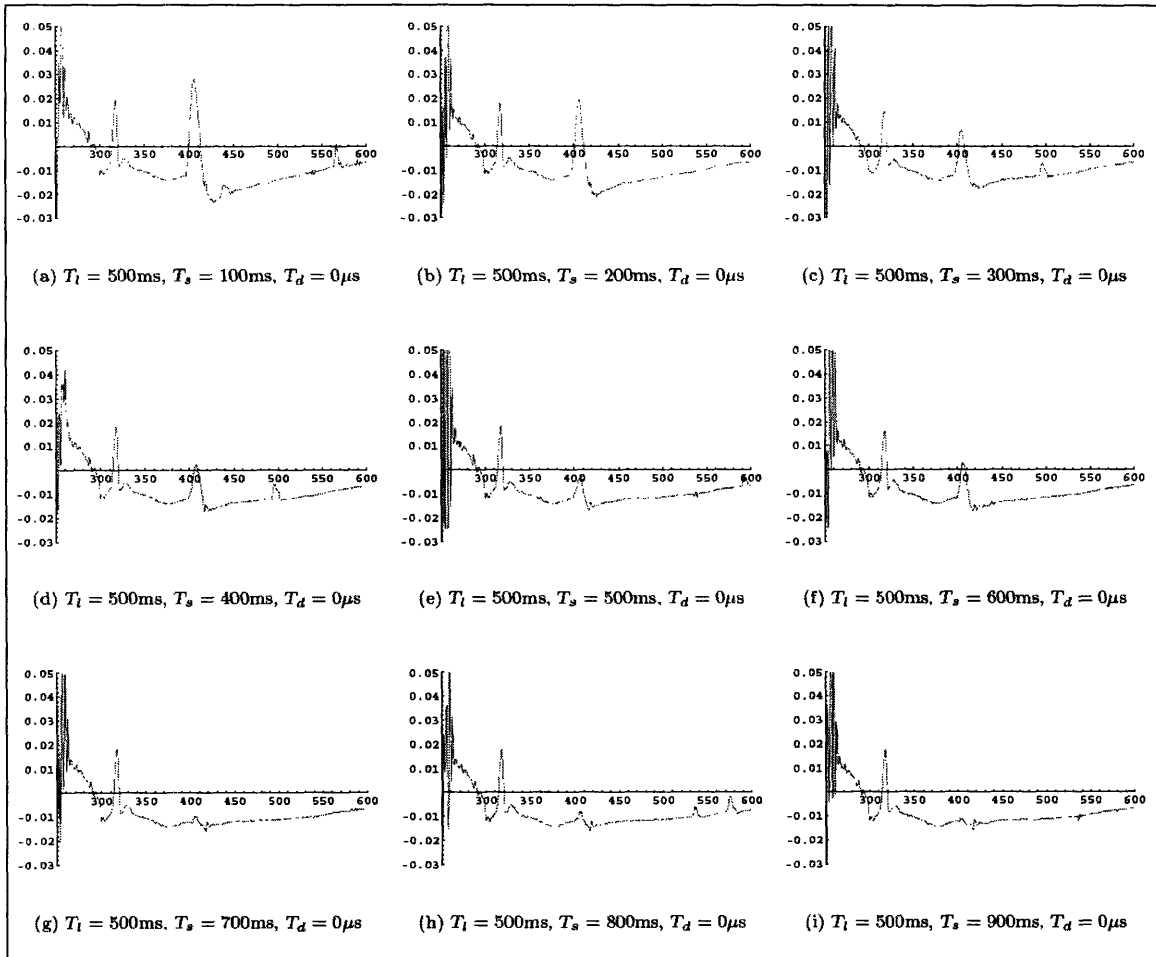


Figure 14 Dependence of trap on Ion Storage Time Increased ion storage time leads to decreased signal.

CHAPTER 4: DISCUSSION

Successfully loading this planar trap from a cold atom source makes available a range of possible applications, both by improving existing technologies and techniques and by probing newly-available possibilities.

In the short-term, there is ample work yet to be done to fully characterize the trap in its current configuration: extend and measure the trap lifetime and determine its limiting factor. Completing the repumping cycle described earlier and applying a cooling laser on the ionic 369nm line holds the potential to dramatically increase the trap lifetime. The resultant ionic fluorescence should allow us to image the trap and confirm the formation of a Wigner crystal of ions along the trap axis. By varying the phase between the trapping electrodes, we should be able to not only move the ions toward or away from the trap, but also study how this distance affects the trap lifetime. We can also explore the relationship between the micro-motion collective heating and the trapping voltages, and by varying the trapping parameters affect and measure the stability of the trap.

In the long-term, having an ion trap that loads from a cold atom cloud and can then be moved allows for some interesting and novel studies, including the interactions of the ions and atoms in the cloud, and the potential for another scale-down in size, incorporating a nested trap within the center electrode of our current trap. In this idea, the MOT provides a cold atom source for the larger ion trap, which then traps, cools, and moves the ions to the trapping location for the smaller ion trap. We can also easily study how the ions' distance from the trap influences the heating rate, the so-called anomalous heating effect.²⁴

As mentioned earlier, $^{171}\text{Yb}^+$ is a strong candidate for qubit operations either on the quadrupole transition at 435nm or particularly on the ground state hyperfine transition at 12.6GHz in the microwave region (see Figure 1).²⁵ Additionally, $^{171}\text{Yb}^+$ is a candidate for optical frequency standards on the clock transition at both 435nm (quadrupole transition) and 467nm (octopole transition) with a theoretical linewidth in the nHz range.²⁶ With the

²⁴ Q. A. Turchette, D. Kielpinski, B. E. King, D. Leibfried, D. M. Meekhof, C. J. Myatt, M.A. Rowe, C. A. Sackett, C. S. Wood, W. M. Itano, C. Monroe, D. J. Wineland, *Phys. Rev. A* **61** 063418 (2000).

²⁵ C. Balzer, A. Braun, T. Hannemann, C. Paape, M. Ettl, W. Neuhauser, and C. Wunderlich, *quant-ph/0602044*.

²⁶ P. Gill, *Metrologia*, **42** S125 (2000)

simplicity and ease of construction and operation outlined here, the loading of surface trap from a cold atom source that we have demonstrated could be a significant enabler for either of these fields.

APPENDIX A: MAGNETIC COILS

Our trapping chamber incorporates two configurations of electromagnetic coils, gradient coils and bias coils.

Gradient Coils

The “Main MOT” coils provide a linear magnetic gradient along each axis in order to Zeeman-split the sub-levels of the excited state of neutral Yb, which in turn contributes to the trapping force, as outlined in Chapter 2. These coils are depicted in Figure A1(a).

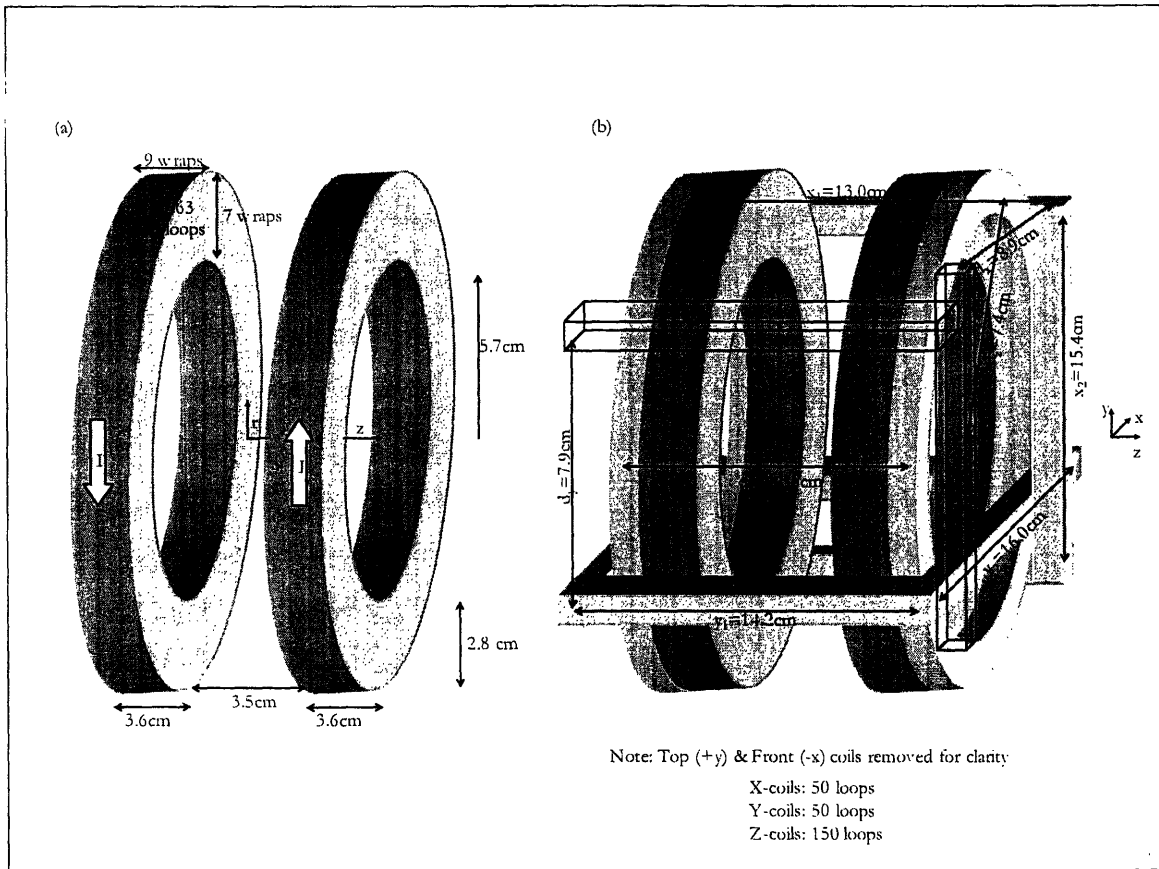


Figure A1. Magnetic Coils (a) Main MOT coils in an anti-Helmholtz configuration. (b) Bias coils along three axes, arranged in an approximately Helmholtz configuration.

They consist of square-profile, insulated copper tubing, which allow water-cooling to dissipate the heat generated by large currents through these coils. Each of the two coils consists of 63 loops of wire, and they are arranged in an approximately anti-Helmholtz configuration, with the current going in opposite directions through the two sets of coils. The magnetic field produced at a point along the z-axis is

$$B(z) = \frac{\mu_0}{2} Ir^2 \left(\frac{1}{\left(r^2 + \left(\frac{d}{2} - z \right)^2 \right)^{\frac{3}{2}}} - \frac{1}{\left(r^2 + \left(\frac{d}{2} + z \right)^2 \right)^{\frac{3}{2}}} \right) N \quad [\text{A1}]$$

where $\mu_0 = 4\pi \times 10^{-7} \text{ N/A}^2$ is the permeability of free space, I is the coil current, r is the radius of a coil, d is the distance separating the sets of coils, and N is the number of turns in each set.

The magnetic field gradient along the z -axis is

$$\partial_z B(z) = \frac{dB(z)}{dz} = \frac{\mu_0}{2} Ir^2 \left(\frac{3\left(\frac{d}{2} - z\right)}{\left(r^2 + \left(\frac{d}{2} - z \right)^2 \right)^{\frac{5}{2}}} - \frac{3\left(\frac{d}{2} + z\right)}{\left(r^2 + \left(\frac{d}{2} + z \right)^2 \right)^{\frac{5}{2}}} \right) N \quad [\text{A2}]$$

which, when $d=r$ and remembering $1 \text{ T}[\text{N/Am}] = 10^4 \text{ G}$, simplifies to

$$\partial_z B(z=0) \left[\frac{\text{G}}{\text{m}} \right] = \frac{3\mu_0 IN}{2\left(\frac{5}{4}\right)^{\frac{5}{2}} r^2} = \frac{.0108 \left[\frac{\text{N}}{\text{A}^2} \right] I[\text{A}] N}{(r[\text{m}])^2} \quad [\text{A3}]$$

From another recent Yb MOT,²⁷ we designed for an optimal value of $\partial_z B(z=0)$ of 45 G/cm, yielding a current of 33A. In practice, we optimized our MOT at 31A or 42 G/cm, although there seems to be a broad range of 25-50A that our MOT can operate in.

Bias Coils

The ‘‘bias’’ coils, depicted in Figure A1(b), provide us with the ability to apply small offset fields along each of the three principle axes. In practice, we use them to adjust the quadrupole center of our main MOT coils’ magnetic field to co-locate it with our trapping laser beam intersection, and hence optimize our MOT’s strength and position.

²⁷ C.Y. Park, and T.H. Yoon, Phys. Rev. A **68**, 055401 (2003).

These coils consist of 20 gauge insulation-coated electromagnet wire. Ideally, they are a Helmholtz configuration with the current flowing in the same direction through both sets of coils, yielding a magnetic field along any principle direction of

$$B(z) = \frac{\mu_0}{2} I r^2 \left[\frac{1}{\left(r^2 + \left(\frac{d}{2} - z \right)^2 \right)^{\frac{3}{2}}} + \frac{1}{\left(r^2 + \left(\frac{d}{2} + z \right)^2 \right)^{\frac{3}{2}}} \right] N = \frac{\mu_0 I r^2}{\left(r^2 + \left(\frac{d}{2} - z \right)^2 \right)^{\frac{3}{2}}} N \quad [\text{A4}]$$

In practice, the coil loops are not round, but rectangular, and the separation distance is only approximately equal to the coil radius ($d \approx r$), due to constraints of fitting the coils around the trapping chamber without blocking optical access. Under this approximation,

$$B(z=0)[G] = \frac{\mu_0 I}{\left(\frac{5}{4} \right)^{\frac{3}{2}} r} N = \frac{.009 I[A] N}{r[m]} \quad [\text{A5}]$$

The coils on all three axes are designed to move the MOT up to three millimeters in either direction against the field gradient of $\partial_z B = 45 \text{ G/cm}$, and from symmetry and divergence arguments, $\partial_{x,y} B = 22.5 \text{ G/cm}$.

Along the z-axis, there is an effective separation of $d = 11.6 \text{ cm}$ and radius of $r = 7.4 \text{ cm}$, yielding $B_z = 14.2 \text{ G/A}$.

Along the y-axis, there is an effective separation of $d = 7.9 \text{ cm}$ and radius of $r = 9.6 \text{ cm}$, yielding $B_y = 5.1 \text{ G/A}$.

Along the x-axis, there is an effective separation of $d = 8.9 \text{ cm}$ and radius of $r = 9.1 \text{ cm}$, yielding $B_x = 5.0 \text{ G/A}$.

The effective radii and separation distances are averages based on the separation of the main part of the coil or on a circular coil loop of the same circumference as our coil loops. In practice, two of our coils (x- and y-directions) are rectangular, and some of them have bends or kinks to allow optical access or to route around other equipment.

Experimentally, current is controlled via a MOSFET-based current controller in which 1V of control voltage yields 1A of coil current. Due to the different lengths and

hence resistances of the coils, the current supplies can provide up to 1.5A current in the z-direction, and 2A current in both the x- and the y-directions.

APPENDIX B: RESPONSE TIMES

The trapping times in the experiment are on the order of 10s to 100s of milliseconds, and useful data from the experiment often needs to be integrated over many data sets. Consequently, it is advantageous to be able to execute the sequence many times a second. Each device in our set-up has characteristic response times from a trigger, and some of these response times are significant enough to limit the repetition speed of the experiment. This Appendix examines the various response times of the equipment.

All triggers in the experiment are currently provided and timed through the data acquisition computer using a SpinCore Technologies, Inc. card, which outputs digital triggers of 0V and 3.3V (low and high respectively).

Ion Detector / High Voltage

The Channeltron 5901 ion detector requires a high negative voltage to attract ions. Originally, this was provided by a Bertan Model 205A-05R 3kV, 5mA power supply, but it seemed to have difficulties providing the current spikes associated with ion counts, and smoothing the current spikes with capacitors seemed to accomplish little. Currently, the ion detector is powered by a Analog Modules, Inc. (Model 829) Pockels' Cell driver, capable of voltage spikes of -3.5kV which can be triggered from digital input. In practice, we found that the output voltage spike occurs 2.5 μ s after the trigger signal. This voltage spike is visible through the ion detector as the large peak on the left of all count rate data.

UV LED

The UV LED is controlled by a MOSFET-based current controller. The speed of this current controller is retarded by an internal capacitance within the LED. At low power, the LED has an 11 μ s turn-on/off delay from its trigger and at full power, the LED has a 19 μ s turn-on/off delay from its trigger.

RF Voltage

The trapping voltages, applied from a Stanford Research Systems DS345 Function Generator and amplified by a Mini-Circuits +30dBm medium-high power amplifier (Model: ZHL-32A), are then stepped up by a resonant inductive-capacitive circuit, so that

approximately 1100V_{pp} are applied to the rf-electrodes. A fast (6ns typical) rf-switch (Mini-Circuits Model ZYSWA-2-50DR) allows turn-on/off of this trapping voltage, which exponentially grows/decays with a half-life of approximately 5 μ s.

Mechanical Shutter

We used a mechanical shutter to block the atom-trapping laser light at 399nm. The shutter is isolated from the optical table to prevent mechanical vibrations on the optical elements. The shutter responds to a high control signal by closing and a low control signal by opening. The shutter begins to close 3ms after a trigger signal and is fully closed by 3.8ms. Opening, the shutter response 4ms after a trigger and is fully open by 4.5ms.

SELECTED BIBLIOGRAPHY

- _____. *Channeltron Electron Multiplier Handbook for Mass Spectrometry Applications*. Burle Technologies, Inc.
- _____. *Basic Atomic Spectroscopic Data*. Aug 2005. <http://physics.nist.gov/PhysRefData/Handbook/Tables/ytterbiumtable1.htm>. Accessed April 22, 2006.
- Balzer, C., A. Braun, T. Hannemann, C. Paape, M. Ettl, W. Neuhauser, and C. Wunderlich. 2006. *quant-ph/0602044*.
- Bell, A. S. P. Gill, H. A. Klein, A. P. Levick, C. Tamm, D. Schrier. 1991. *Laser cooling of trapped ytterbium ions using a four-level optical-excitation scheme*. *Phys. Rev. A* **44** R20-R23.
- Chiaverini, J., R. B. Blakestad, J. Britton, J. D. Jost, C. Langer, D. Leibfried, R. Ozeri, and D. J. Wineland. 2005. *Surface-Electrode Architecture for Ion-Trap Quantum Information Processing*. *Quantum Information and Communication*, **5**, 419-439.
- Corwin, K. L., Z. T. Lu, C. F. Hand, R. J. Epstein, C. E. Wieman. 1998. *Frequency-stabilized diode laser with the Zeeman shift in an atomic vapor*. *Appl. Op.* **37** 3295.
- Das, D., S. Barthwal, A. Banerjee, and V. Natarajan. 2005. *Absolute frequency measurements in Yb with .08ppb uncertainty: Isotope shifts and hyperfine structure in the 399-nm 1S_0 - 1P_0 line*. *Phys. Rev. A* **72** 032506.
- Dehmelt, H. G. 1967. *Radiofrequency Spectroscopy of Stored Ions I: Storage*. In *Advances in Atomic and Molecular Physics*. Ed. D. R. Bates, I. Estermann. New York: Academic Press.
- DiVinzenco, D. P. 2000. *The Physical Implementation of Quantum Computation*. *Fortschr. Phys.* **48**. 771-783.
- Eschner, J., G. Morigi, F. Schmidt-Kaler, R. Blatt. 2003. *Laser cooling of trapped ions*. *J. Opt. Soc. Am. B* **20** 1003.
- Gill, Patrick. 2005. *Optical frequency standards*. *Metrologia* **42** S125.
- Ghosh, P. K. 1995. *Ion Traps*. Oxford: Clarendon Press.
- Hawthorn, C. J., K. P. Weber, and R. E. Scholten. 2001. *Littrow configuration tunable external cavity diode laser with fixed direction output beam*. *Rev. Sci. Instr.* **72** 4477.
- Horowitz, P., and W. Hill. 1989. *The Art of Electronics*. 2nd Ed. Cambridge: Cambridge University Press.
- Janik, G. R., J. D. Prestage, and L. Maleki. 1990. *Simple analytic potentials for linear ion traps*. *J. Appl. Phys.* **67** 6050.
- Kim, J. I., C. Y. Park, J. Y. Yeom, E. B. Kim, T. H. Yoon. 2003. *Frequency-stabilized high-power violet laser diode with an ytterbium hollow-cathode lamp*. *Opt. Lett.* **28** 245-247.
- Letokhov, V. S. 2002. *Electromagnetic Trapping of Cold Atoms: An Overview*. In *Trapped Particles and Fundamental Physics*. Ed. S.N. Atutov, R. Calabrese, and L. Moi. Dordrecht, The Netherlands: Kluwer.
- March, R. E. and J. F. J. Todd. 2005. *Quadrupole Ion Trap Mass Spectrometry*. 2nd Ed. Hoboken, New Jersey: Wiley-Interscience.
- Metcalf, H. J. and P. van der Straten. 1999. *Laser Cooling and Trapping*. New York: Springer. 87-90, 156-158.
- Park, C. Y. and T. H. Yoon. 2003. *Efficient magneto-optical trapping of Yb atoms with a violet laser diode*. *Phys. Rev. A* **68** 055401.
- Paul, W. 1989. *Electromagnetic Traps for Charged and Neutral Particles*. Nobel Lecture.

- Pearson, C. E., D. R. Leibbrandt, W. S. Bakr, W. J. Mallard, K. R. Brown, and I. L. Chuang. 2006. *Experimental investigation of planar ion traps*. Phys. Rev. A **73** 032307.
- Raab, E. L., M. Prentiss, A. Cable, S. Chu, and D. E. Pritchard. 1987. *Trapping of Neutral Sodium Atoms with Radiation Pressure*. Phys. Rev. Lett. **59** 2631.
- Roberts, M., P. Taylor, G. P. Barwood, W. R. C. Rowley, and P. Gill. 2000. *Observation of an Electric Octupole Transition in a Single Ion*. Phys. Rev. A **62** 020501.
- Seidelin, S., J. Chiaverini, R. Reichle, J. J. Bollinger, D. Leibfried, J. Britton, J. H. Wesenberg, R. B. Blakestad, R. J. Epstein, D. B. Hume, J. D. Jost, C. Langer, R. Ozeri, N. Shiga, and D. J. Wineland. 2006. *A microfabricated surface-electrode ion trap for scalable quantum information processing*. quant-ph/0601173. Accessed: May 1, 2006.
- Siegman, A. E. 1986. Lasers. Sausalito, California: University Science Books.
- Steane, A. 1997. *The ion trap quantum information processor*. Appl. Phys. B **64** 623-642.
- Svelto, Orazio. 1998. *Principles of Lasers*. 4th Ed. Trans. David C. Hanna. New York: Plenum Press.
- Todd, J. F. J. 1995. *Ion Trap Theory, Design, and Operation*. Practical Aspects of Ion Trap Mass Spectrometry, Vol. III. Ed. R. E. March, J.F.J. Todd. Boca Raton, Florida: CRC Press.
- Warrington, R. B., P. T. H. Fisk, M. J. Wouters, M. A. Lawn, J. S. Thorn, S. Quigg, A. Gajaweera, and S. J. Park. 2005. *Time and Frequency Activities at the National Measurement Institute, Australia*. Proceedings of the Asia-Pacific Time and Frequency 2000 Workshop. IEEE.
- Yashchuk, V., D. Budker, and J. Davis. 2000. *Laser Frequency Stabilization Using Linear Magneto-Optics: Technical Notes*. Rev. Sci. Instr. **71** 341.
- Yoda, J. and K. Sugiyama. 1992. *Disappearance of trapped Yb^+ ions by irradiation of the resonance radiation*. J. Mod. Op. **39** 403-409.